This number is one-seventh of the value reported in (*1*) as the upper limit of viscosity of superfluid helium. For comparison, the viscosity of normal fluid $^4$He is $2 \times 10^{-6}$ Pa·s. This calculation invalidates this soft shear mode interpretation and supports the superflow interpretation.

The smooth decay in $\rho_s/\rho$ with increasing temperature near 250 mK makes it difficult to determine with precision the supersolid transition temperature $T_c$. We estimate the value of $T_c$ by assuming a linear dependence of $\rho_s/\rho$ on temperature near $T_c$ and then use the data with $\rho_s/\rho$ between 0.01 and 0.1 to fit for $T_c$. The resultant transition temperatures, with uncertainty of 20 mK, are likely to be lower than the "true" values. The transition temperatures we have found show a weak pressure dependence decreasing from 315 mK at 26 bars down to 230 mK at pressures exceeding 40 bars. The phase diagram of $^4$He, including both the superfluid and supersolid phases, is shown in Fig. 4.

A number of experiments have searched for the supersolid phase in bulk solid helium without success (*27*). A recent experiment found an unexpected interaction between acoustic and heat pulses in solid $^4$He with several tens of parts per million of $^3$He (*28*). The result led to the interpretation of a Bose condensate of thermally activated vacancies at temperatures above 200 mK and therefore is not related to the findings reported here. A prior torsional oscillator experiment (*29*) reported the absence of any supersolid decoupling in a solid $^4$He sample that contains 411 parts per million of $^3$He—a concentration, as we found in the Vycor experiment (*15*), sufficient to quench the supersolid phase. The authors of this prior experiment also reported that they failed to find evidence of the supersolid phase in samples of high-purity $^4$He (*29*). Our results disagree with this conclusion. Other experiments involve the search of motion of a falling dense object in solid helium or flow of solid helium from one chamber of higher pressure to one of lower pressure (*30–34*). A likely explanation of why these experiments found null results is that such pressure-driven mass flow requires a difference in the supersolid fraction between regions or chambers of different pressures. Our measurements showed that the supersolid fraction is insensitive to the pressure of the solid $^4$He samples.

We noted above that Bose-Einstein condensation is found together with superfluidity in bulk liquid helium and in alkali gases. In contrast, superfluidity at $T > 0$ is found in two-dimensional liquid helium films without Bose-Einstein condensation (*18*). An intriguing question is whether the supersolid phase is associated with Bose-Einstein condensation.


**References and Notes**

1. P. Kapitza, *Nature* **141**, 74 (1938).
2. J. F. Allen, A. D. Misener, *Nature* **141**, 75 (1938).
3. P. Nozières, D. Pines, *Theory of Quantum Liquids* (Addison-Wesley Reading, MA, 1989), vol. 2, chap. 6.
4. P. E. Sokol, in *Bose-Einstein Condensation*, A. Griffin, D. W. Snoke, S. Stringari, Eds. (Cambridge Univ. Press, Cambridge, 1995).
5. M. Anderson, J. R. Ensher, M. R. Matthews, C. E. Wieman, E. A. Cornell, *Science* **269**, 198 (1995).
6. M. R. Matthews *et al.*, *Phys. Rev. Lett.* **83**, 2498 (1999).
7. A. P. Chikkatur *et al.*, *Phys. Rev. Lett.* **85**, 483 (2000).
8. F. Chevy, K. W. Madison, J. Dalibard, *Phys. Rev. Lett.* **85**, 2223 (2000).
9. A. F. Andreev, I. M. Lifshitz, *Sov. Phys. JETP* **29**, 1107 (1969).
10. G. V. Chester, *Phys. Rev. A.* **2**, 256 (1970).
11. A. J. Leggett, *Phys. Rev. Lett.* **25**, 1543 (1970).
12. K. S. Liu, M. E. Fisher, *J. Low Temp. Phys.* **10**, 655 (1973).
13. M. Liu, *Phys. Rev. B* **18**, 1165 (1978).
14. D. E. Galli, L. Reatto, *J. Low Temp. Phys.* **124**, 197 (2001).
15. E. Kim, M. H. W. Chan, *Nature* **427**, 225 (2004).
16. J. R. Beamish, *Nature* **427**, 204 (2004).
17. D. J. Bishop, J. D. Reppy, *Phys. Rev. Lett.* **40**, 1727 (1978).
18. J. M. Kosterlitz, D. J. Thouless, *J. Phys. C* **6**, 1181 (1973).
19. V. Ambegaokar, B. I. Halperin, D. R. Nelson, E. D. Siggia, *Phys. Rev. Lett.* **40**, 783 (1978).
20. A. L. Fetter, *J. Low Temp. Phys.* **16**, 533 (1974).
21. E. J. Mueller, personal communication.
22. R. P. Feynman, in *Progress in Low Temperature Physics I* (North-Holland, Amsterdam, 1955), chap. 2.
23. J. F. Fernandez, M. Puma, *J. Low Temp. Phys.* **17**, 131 (1974).
24. R. A. Guyer, *Phys. Rev. Lett.* **26**, 174 (1970).
25. W. M. Saslow, *Phys. Rev. Lett.* **36**, 1151 (1976).
26. D. Ceperley, G. V. Chester, M. H. Kalos, *Phys. Rev. B* **17**, 1070 (1978).
27. M. W. Meisel, *Physica B* **178**, 121 (1992).
28. J. M. Goodkind, *Phys. Rev. Lett.* **89**, 095301 (2002).
29. D. J. Bishop, M. A. Paalanen, J. D. Reppy, *Phys. Rev. B* **24**, 2844 (1981).
30. A. Andreev, K. Keshishev, L. Mezhov-Deglin, A. Shal'nikov, *Pis'ma Zh. Eksp. Teor. Fiz.* **9**, 507 (1969) [*Sov. Phys. JETP Lett.* **9**, 306 (1969)].
31. V. L. Tsymbalenko, *Pis'ma Zh. Eksp. Teor. Fiz* **23**, 709, (1976) [*Sov. Phys. JETP Lett.* **23**, 653 (1976)].
32. D. S. Greywall, *Phys. Rev. B* **16**, 1291 (1977).
33. G. Bonfait, H. Godfrin, B. Castaing, *J. Phys. (Paris)* **50**, 1997 (1989).
34. N. E. Dyumin, S. V. Svatko, V. N. Grigor'ev, *Fiz. Nizk. Temp.* **15**, 524 (1989).



35. We thank J. R. Banavar, J. R. Beamish, D. J. Bishop, M. E. Fisher, J. M. Goodkind, J. K. Jain, A. J. Leggett, E. Mueller, M. A. Paalanen, J. D. Reppy, W. M. Saslow, K. Shirahama, and D. S. Weiss for informative discussions. Supported by the NSF Condensed Matter Physics Program.


**Supporting Online Material**

www.sciencemag.org/cgi/content/full/1101501/DC1
Fig. S1


15 June 2004; accepted 12 August 2004
Published online 2 September 2004;
10.1126/science.1101501
Include this information when citing this paper.


# Visualization of Dislocation Dynamics in Colloidal Crystals


**Peter Schall,[1]* Itai Cohen,[1,2] David A. Weitz,[1,2] Frans Spaepen[1]**



**The dominant mechanism for creating large irreversible strain in atomic crystals is the motion of dislocations, a class of line defects in the crystalline lattice. Here we show that the motion of dislocations can also be observed in strained colloidal crystals, allowing detailed investigation of their topology and propagation. We describe a laser diffraction microscopy setup used to study the growth and structure of misfit dislocations in colloidal crystalline films. Complementary microscopic information at the single-particle level is obtained with a laser scanning confocal microscope. The combination of these two techniques enables us to study dislocations over a range of length scales, allowing us to determine important parameters of misfit dislocations such as critical film thickness, dislocation density, Burgers vector, and lattice resistance to dislocation motion. We identify the observed dislocations as Shockley partials that bound stacking faults of vanishing energy. Remarkably, we find that even on the scale of a few lattice vectors, the dislocation behavior is well described by the continuum approach commonly used to describe dislocations in atomic crystals.**


Dislocations in a crystalline lattice are central to our understanding of yield, work hardening, fracture, fatigue, and time-dependent elasticity in atomic crystals (*1*). Such dislocations are line defects that mark the boundary of a surface at which one part of the crystal has been uniformly translated with respect to the other (*2–4*). A complete understanding of dislocations and their dynamics requires an analysis that bridges a range of length scales (*5*). On the atomic scale, the interatomic potential determines the structure of the dislocation core. On the medium-range scale, the strain field of the dislocations determines their interactions. On the macroscopic scale, the behavior of the dislocations determines the deformation of the crystal. It is difficult to observe dis-


[1]Division of Engineering and Applied Sciences, [2]Department of Physics, Harvard University, 9 Oxford Street, Cambridge, MA 02138, USA.

*To whom correspondence should be addressed. E-mail: pschall@deas.harvard.edu

locations simultaneously on these length scales. Transmission electron microscopy (TEM) is best suited for in situ observations on the medium-range scale. Computer simulations can bridge the length scales, but the size of their systems and length of the evolution time remain limited. Thus, there remains a need for techniques that link investigations of dislocations on these different length scales.

We show that colloidal crystals offer a unique opportunity for just such a bridging of length scales. Because colloidal particles are several orders of magnitude larger than atoms, they can be studied in real time and their positions in three dimensions can be determined accurately by confocal microscopy (*6*). Concentrated hard-sphere colloidal suspensions form crystals to increase their entropy, thereby lowering their free energy. Such crystals have a finite stiffness (*7*), which is essential for the existence of dislocations. To study these dislocations on the medium scale, we developed a laser diffraction microscopy (LDM) technique that images the strain field in a manner analogous to TEM in atomic systems. Confocal microscopy and LDM make a powerful combination for studying dislocation dynamics simultaneously over two qualitatively different length scales.

We focus on misfit dislocations formed when a film is grown via particle sedimentation on a substrate with a different lattice parameter. This configuration allows us to introduce the dislocations in a controlled way and to study nucleation and propagation of dislocations (*8*) during a process analogous to the industrially important epitaxial growth of thin atomic crystalline films. In thin epitaxial films, the misfit strain $\varepsilon_0$ is accommodated purely elastically and results in a uniform strain $\varepsilon_{el}$. The total elastic energy increases linearly with the film thickness. At some critical thickness $h_c$, the crystal can lower its energy by incorporating dislocations that relieve some of the elastic strain. As the film thickness increases, an increasing portion of the misfit strain is accommodated.

We determine the important parameters of the dislocation array: number per length, Burgers vector, position and range of the strain field, and mobility. We find that many of these features can be accounted for by the continuum theory used for epitaxial growth of atomic thin films. Some features, however, are unique to colloidal crystals, such as the negligibly small stacking fault energy and the slight variation of the lattice parameter with height (due to the pressure head of the upper layers).

We grow colloidal face-centered cubic (fcc) single crystals by slowly sedimenting colloidal particles onto a patterned template (*9*). We use silica particles with a diameter of 1.55 μm and a polydispersity of less than 3.5% (*10*). We prepare a pattern (*11*) with lattice constant $d_0$ = 1.63 μm that nearly matches the equilibrium interparticle separation for colloidal crystals that are about 30 μm thick. This preferred lattice spacing changes slightly with film thickness as a result of the difference in the pressure head (*12*).

We add 3.5 ml of the dilute suspension, which after sedimentation gives rise to about 11 crystalline layers corresponding to a film 13 μm thick. After several days, we remove two-thirds of the supernatant and replace it with another dose of the dilute silica suspension. Using this procedure, we grow the crystal by 9-μm increments until the film is 31 μm thick.

We image dislocations in the crystalline films with a simple LDM setup that is inspired by the TEM techniques used to investigate dislocations in atomic systems (*13*). We use a HeNe laser with a wavelength of 632 nm, which scatters coherently from the colloidal crystal. When the incident beam is perpendicular to the template, a symmetric fcc (100) diffraction pattern is observed. By slightly tilting the sample to change the direction of the incident beam, we maximize the intensity in the (220) diffracted spot. We then use two lenses to project the light in the diffracted beam onto a screen (Fig. 1A). The image on the screen corresponds to a region in the crystal that is illuminated by the incident beam. A perfect crystal shows a uniformly bright image. When the crystal contains dislocations, however, dark lines appear in the image: The bending of lattice

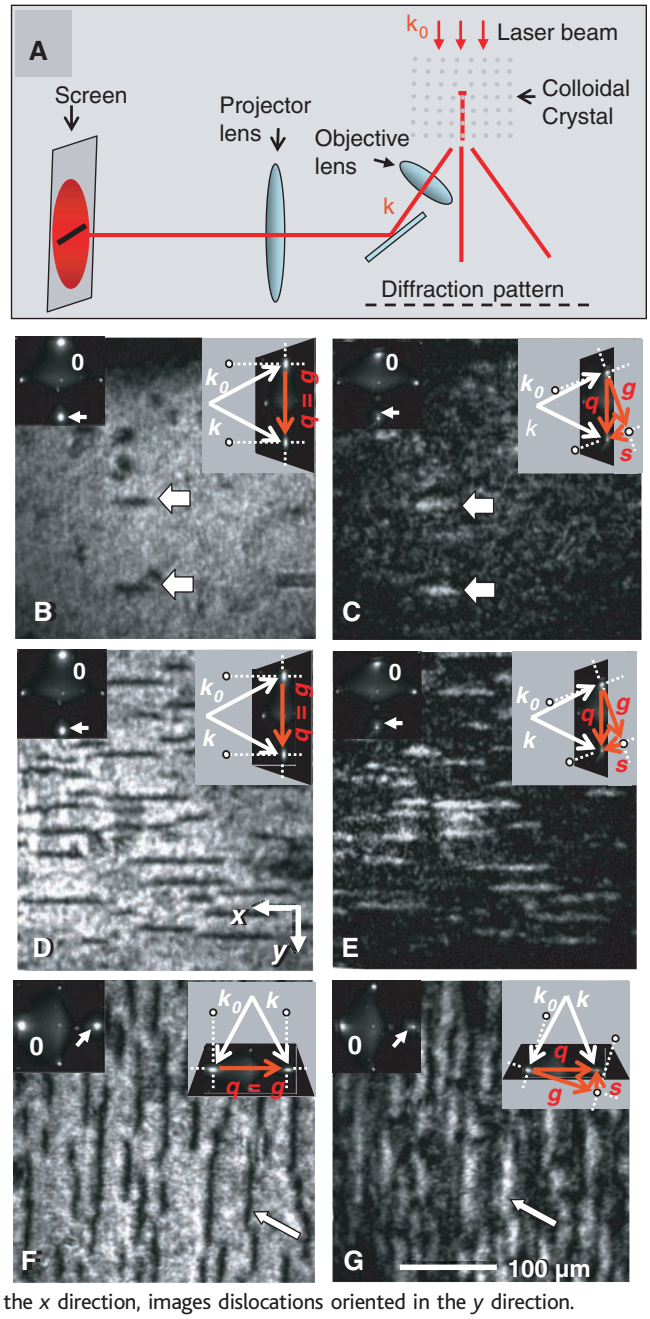


**Fig. 1.** Laser diffraction microscopy (LDM) technique and images. (**A**) Schematic of the LDM instrument: A laser beam is sent through a colloidal crystal. One of the diffracted beams is imaged on a screen by means of an objective and a projector lens. (**B** and **C**) LDM images of the colloidal crystal grown on the template with the ideal lattice constant $d_0$ = 1.63 μm. Arrows indicate dislocations. The upper left inset shows the diffraction pattern from the crystalline film; 0 indicates the transmitted beam, and an arrow indicates the diffracted beam used for imaging. The upper right inset illustrates the wave vectors of the incident and diffracted beams $\mathbf{k}_0$ and $\mathbf{k}$, the diffraction vector $\mathbf{q} = \mathbf{k} - \mathbf{k}_0$, and the corresponding reciprocal lattice vector $\mathbf{g}$. In (B) the diffraction vector $\mathbf{q}$ coincides with the reciprocal lattice vector $\mathbf{g}$ and the diffracted beam intensity is maximum. In (C), the sample is tilted, so that $\mathbf{q}$ differs from $\mathbf{g}$ by the excitation error $\mathbf{s} = \mathbf{q} - \mathbf{g}$, which gives rise to an inversion of the image contrast. (**D** to **G**) LDM images of a colloidal crystalline film grown on a stretched template with lattice constant $d_1$ = 1.65 μm. (D) and (E) show that using the (220) diffraction vector, which lies along the *y* direction, gives images of dislocations oriented in the *x* direction. (F) and (G) show that choosing the $(\bar{2}20)$ diffraction vector, which lies along the *x* direction, images dislocations oriented in the *y* direction.

planes in the strain field of the dislocation gives rise to a local change in the Bragg condition and results in a dark line in the image of the diffracted beam. A LDM image of a 0.3 mm by 0.3 mm section of the colloidal crystal grown on the template with the ideal lattice constant $d_0$ = 1.63 μm is shown in Fig. 1B. Even these crystals, grown on templates with an ideal lattice constant, contain some dislocations (indicated by arrows). Such dislocations are most frequently observed near the template border.

We can further exploit the analogy with the TEM technique and use contrast inversion to verify that the dark lines in Fig. 1B indeed result from scattering due to the dislocations. When the sample is tilted slightly further, the Bragg condition is no longer fulfilled in the perfect lattice and is instead locally satisfied in the region corresponding to the dislocation strain field. Thus, the image contrast on the screen inverts (Fig. 1C). The additional tilt of the sample introduces an excitation error, $\mathbf{s} = \mathbf{q} - \mathbf{g}$ (Fig. 1C, upper right inset), which causes the intensity in the diffracted beam to decrease (Fig. 1C, upper left inset). Close to the dislocation, however, the bending of lattice planes locally scatters light into the direction of the diffracted beam, making the dark lines appear light.

To investigate the effect of a lattice mismatch, we grew a crystal on a template with lattice constant $d_1$ = 1.65 μm, which is 1.5% larger than $d_0$. The crystal grown on the stretched template exhibited a similarly low density of dislocations at a crystal thickness of 22 μm. Strikingly, as the crystal was grown to a thickness of 31 μm, a large number of dislocations nucleated and grew (Fig. 1, D and E). We determined the average dislocation line separation in the direction perpendicular to the dislocation lines, Λ, from the images. $\Lambda^{-1}$ is the number of dislocations per unit length. Measuring Λ in three different 0.3 mm by 0.3 mm regions, we obtained an average value of 53 (±10) μm for the 31-μm crystal.

Remarkably, although the template was stretched in both spatial directions, dislocation lines were seen in one direction only (Fig. 1, D and E). The dislocation contrast is visible only if the particle displacements in the dislocation strain field have a component parallel to the diffraction vector used for imaging. The (220) diffraction vector chosen for imaging in Fig. 1, B to E, lies along the *y* direction; therefore, only lattice distortions with a component along the *y* direction showed up in the image. When we instead chose the $(\bar{2}20)$ diffraction vector, which lies along the *x* direction, we observed a second set of dislocations (Fig. 1, F and G). Comparing the images in Fig. 1, D and F, we conclude that the strain field of the dislocations is strictly perpendicular to the imaged dislocation lines.

To elucidate the defect structure on the microscopic scale, we used confocal microscopy to image the individual particles and to determine their positions (*6*). The 31-μm-thick fcc colloidal crystal grown on the stretched template contains characteristic defects. At these defects, the nearest neighbor particle configuration changes so that particles have three opposing nearest neighbor pairs, as is the case in the hexagonal close-packed (hcp) lattice, rather than six as in the fcc lattice. A reconstruction of a 55 μm by 55 μm by 17 μm section of the crystal is shown in Fig. 2A. The *x*, *y*, and *z* axes correspond to the $(1\bar{1}0)$, (110), and (001) directions of the fcc lattice, respectively. Particles with three opposing nearest neighbor pairs are shown in red, and those with six opposing nearest neighbor pairs in blue. The red particles lie along intersecting planes embedded in the fcc lattice. By displaying only the red particles, we show that the planes are hcp (Fig. 2B). The red planes sandwich a stacking fault where the stacking order of the hcp planes changes from *ABC-ABCABC* to *ABCBCABCA*. The stacking fault lies along the (111) plane where the dislocations move most easily as a result of the shallow potential wells. This defines the glide plane of the dislocations in the fcc structure.

For a closer look at the strain field associated with the stacking faults, we display a typical *y*-*z* cut through a stacking fault. The fault ends above the template and is terminated by a dislocation (Fig. 2C). The first row of particles sits in the template holes. In the second row of particles, we recognize the emergence of a strain field in the *y*-*z* plane associated with a dislocation line oriented perpendicular to this plane. The dislocation core (⊥) lies about two lattice constants above the template. The Burgers circuit illustrated by the red line, which would close in the perfect lattice, exhibits a closure failure around the dislocation core. The Burgers vector **b**, which connects the starting and ending points of the Burgers circuit, is $1/6(\bar{1}\bar{1}2)$. This type of dislocation is known as a Shockley partial dislocation and is the most prominent dislocation observed in fcc

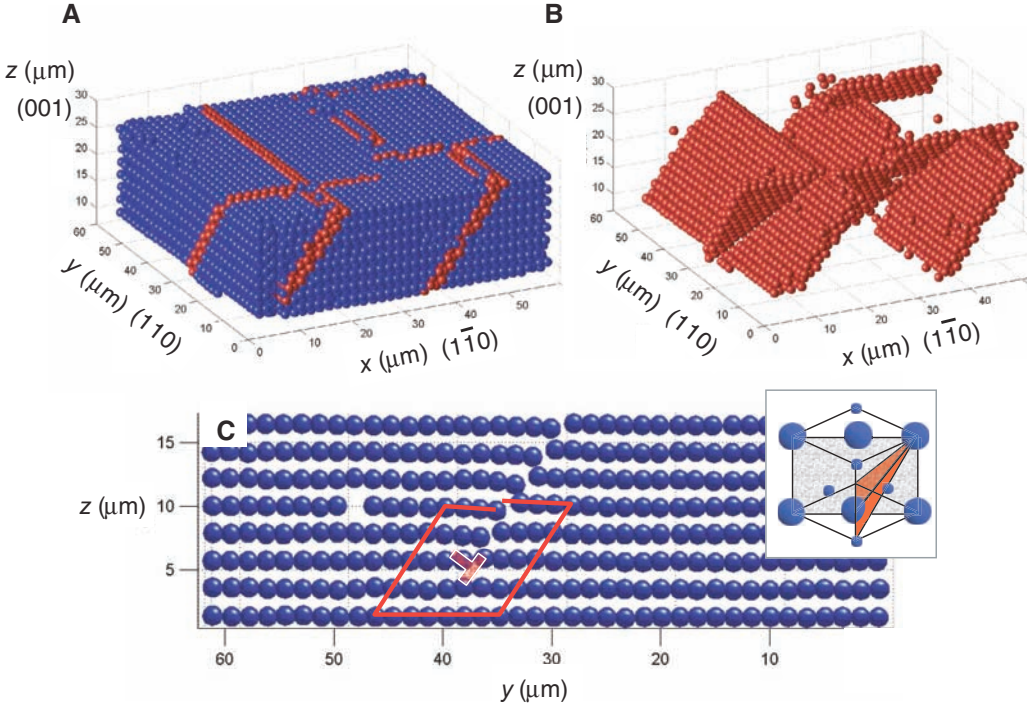


**Fig. 2.** (**A**) Reconstruction of a 55 μm by 55 μm by 17 μm section of the colloidal crystal grown on the stretched template. The red particles delineate stacking faults embedded in an otherwise perfect fcc lattice. (**B**) Crystal reconstruction showing only the particles adjacent to the stacking faults. (**C**) A reconstructed *y*-*z* section through a stacking fault. The stacking fault is terminated by a Shockley partial dislocation whose core position is indicated by ⊥. The red loop indicates a Burgers circuit. The upper right inset is a three-dimensional illustration of the fcc unit cell. The *y*-*z* plane is gray; the hcp plane parallel to the stacking fault is red.

metals (*14*). In metals, Shockley partial dislocations usually appear in pairs, held together by a stacking fault of nonzero energy. In contrast, in the hard-sphere colloidal crystal, the stacking faults extend to the crystal surface. This difference results from the vanishingly low energy cost associated with stacking faults in hard-sphere crystals (*15*), where second nearest neighbor interactions are almost negligible.

To calculate the critical film thickness $h_c$, where the crystal starts to nucleate dislocations in order to relieve some of the elastic strain, we consider the crystalline film to be an isotropic, linear elastic medium with Young modulus $E$, shear modulus $\mu$, and Poisson ratio $\nu$. The widely used one-dimensional dislocation models for misfit dislocations in atomic thin films (*16*, *17*) give $h_c = \mu b \ln(R/r_c)/[4\pi E\varepsilon_0(1-\nu)\cos\alpha]$, where $r_c$ and $R$ are the core and outer radii of the dislocation strain field, respectively (*18*), $\varepsilon_0$ is the misfit strain imposed by the template, and $\alpha$ is the angle between the Burgers vector and its projection onto the template. We take $r_c$ to be $b/4$ (*1*, *19*), $R$ to be the film thickness (*17*), and $\varepsilon_0$ to be 0.015. Because $E/\mu = 2(1+\nu)$ for an isotropic elastic medium (*1*) and the Poisson ratio can be set at $\nu = 1/3$ (*7*), we find $h_c = 22$ μm. Consistent with this prediction, at a thickness of 22 μm the colloidal crystalline film is still free of dislocations. However, as the film thickness is increased to 31 μm, the film develops a large number of dislocations (Fig. 1, D to G), again consistent with the model. The misfit strain associated with the dislocations is $\varepsilon = b\cos\alpha/\Lambda$. Using $b = 0.94$ μm, $\cos\alpha = 1/\sqrt{3}$, and $\Lambda = 53$ μm, we find $\varepsilon = 0.010$, which corresponds to two-thirds of the total misfit strain $\varepsilon_0 = 0.015$ (*20*).

A further test of the continuum model is to calculate the height at which the dislocations rest above the template. A dislocation is driven toward the template by the force $F_{el} = \frac{1}{2}\Lambda E\varepsilon_0^2$, which results from the elastic stress in the layers below the dislocation core, which are still strained (*21*). The boundary condition, set by the requirement that the particles in the first layer must adopt the template spacing, gives rise to an image force that repels the dislocation away from the template. The image force acting on a dislocation whose Burgers vector $\mathbf{b}'$ is parallel to the template and whose core rests at a distance $z$ above the template is $F_i = \mu b'^2/[4\pi(1-\nu)z]$ (*1*). We estimate this force for our system by neglecting the vertical component of the Burgers vector and taking $b' = b\cos\alpha$. The image force balances the elastic force when the dislocation rests at a distance $z_0 = \mu(b\cos\alpha)^2/[2\pi\Lambda E(1-\nu)\varepsilon_0^2]$ from the template. Using $\Lambda = 53$ μm, $b = 0.94$, $\cos\alpha = 1/\sqrt{3}$, and $\varepsilon_0 = 0.015$, we find $z_0 = 2.1$ μm, in good agreement with our observation of $z_0 = 3$ μm. Thus, surprisingly, the predictions of continuum theory, which are typically applied on length scales above 100 lattice constants, hold even for a very small number of layers.

We also used LDM to study the dislocation dynamics during the epitaxial growth of the film. We started with a crystal 22 μm thick, added a final dose of particles, waited 14 hours, and then tracked the evolution of dislocations over a period of 2.5 hours (movie S1). Three snapshots from the movie are shown in Fig. 3, A to C. The images show the spreading of existing dislocations and the nucleation and growth of new ones. Figure 4A shows the dislocation length as a function of time for the four dislocations indicated in Fig. 3C. Initially, the dislocations grow rapidly, at a rate of about 1 μm $s^{-1}$. As the dislocation length increases, however, the growth rate decreases and eventually falls to zero.

To quantitatively analyze this spreading behavior, it is necessary to account for the forces acting on a dislocation. A diagram depicting a typical dislocation line in our thin film is shown in Fig. 4B. The dislocation consists of an edge segment that runs parallel to the template and joins two screw segments that terminate at the crystal surface. The edge dislocation expands through the lateral motion of the screw segments (*22*). Figure 4B also depicts the forces acting on one of the screw segments. The expansion of a dislocation is driven by the Peach-Koehler force $F_{PK}$ due to the elastic stress (*22*) and is resisted by the dislocation line tension $F_l$ (*1*) and a drag force $F_d$ associated with moving the screw segment through the crystal. For colloidal crystals, $F_d$ has been shown to be

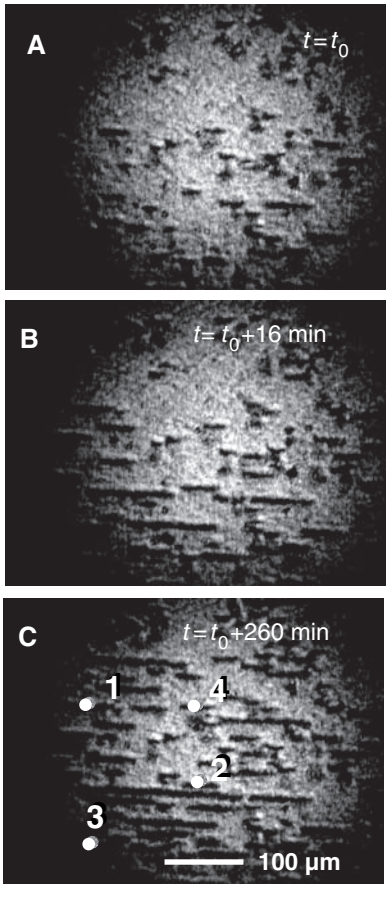


**Fig. 3.** (**A** to **C**) Snapshots from an LDM movie (movie S1) taken during the epitaxial growth of a colloidal crystal film grown on the stretched template. The time $t_0$ corresponds to 14 hours after adding a final dose of particles. The dots in (C) mark four dislocations whose growth is tracked and displayed in Fig. 4.

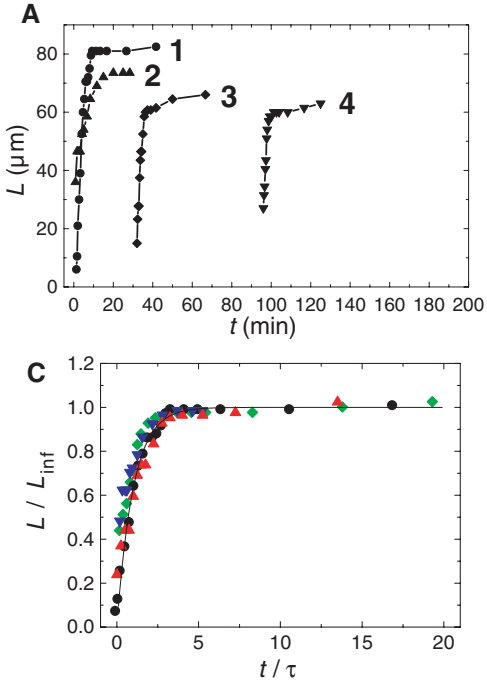


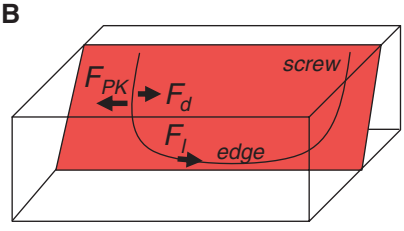


**Fig. 4.** (**A**) Length versus time for the four dislocations marked in Fig. 3C. (**B**) Schematic diagram of a dislocation line that lies in a hcp plane shown in red. The dislocation edge segment runs parallel to the template and joins two screw segments that terminate at the crystal surface. The forces acting on the dislocation line are marked. (**C**) The symbols indicate the rescaled dislocation length $L/L_{inf}$ versus rescaled time $t/\tau$ for the four growth curves marked in (A). The solid line is the theoretical prediction of the model and has the functional form $[1-\exp(t/\tau)]$.

the dominant force associated with the motion of such screw dislocations (*19*). At the onset of dislocation growth, we estimated the magnitude of each of the forces to be on the order of 100 fN. The length of a dislocation as a function of time can be calculated from the force balance, $F_{PK} = F_l + F_d$ (*23*). As the dislocation grows and accommodates an increasing portion of the misfit strain, the elastic force driving the expansion decreases. Thus, the force balance predicts that $L = L_{inf}[1 - \exp(-t/\tau)]$, where $L_{inf}$ is the final dislocation length and $\tau$ is a constant, proportional to the ratio of the viscosity of the solvent to the elastic modulus.

To test this prediction, we scaled the entire data set and plotted $L/L_{inf}$ versus $t/\tau$ (Fig. 4C). The data are in excellent agreement with the theoretical prediction. As a final check, we used the average value of $\tau$, which we determined to be 130 (±40) s, to estimate the elastic modulus of the colloidal crystal (*23*). This estimate yields a value of 0.3 Pa, in reasonable agreement with theoretical estimates that predict a value on the order of 1 Pa (*7*). This is one of the only techniques available for directly determining the elastic modulus of thin colloidal crystal films.

The combination of imaging techniques presented and the close similarity of dislocations in colloidal and atomic crystals lays the groundwork for investigating further important phenomena that cannot be directly studied on the atomic scale, such as the nucleation and interaction of dislocations in very constrained systems. The remarkable and unexpected correspondence between continuum model predictions and the phenomena we observe on the scale of just a few lattice constants suggests that continuum models may also be applied to describe dislocation behavior even in highly constrained structures, such as those being made as nanoscale science pushes to ever smaller devices. Finally, the effects of the vanishing stacking fault energy and the pressure head on dislocations in colloidal crystals highlight some of the unique features of this class of condensed matter.

### References and Notes


1. J. P. Hirth, J. Lothe, *Theory of Dislocations* (Wiley, New York, ed. 2, 1982).
2. G. I. Taylor, *Proc. R. Soc. A* **145**, 362 (1934).
3. E. Orowan, *Z. Phys.* **89**, 605 (1934).
4. M. Polanyi, *Z. Phys.* **89**, 660 (1934).
5. J. Lepinoux, D. Maziere, V. Pontikis, G. Saada, Eds., *NATO Science Series E, Multiscale Phenomena in Plasticity: From Experiments to Phenomenology, Modeling and Materials Engineering* (Kluwer Academic, Dordrecht, Netherlands, 2000), vol. 367.
6. A. D. Dinsmore, E. R. Weeks, V. Prasad, A. C. Levitt, D. A. Weitz, *Appl. Opt.* **40**, 4152 (2001).
7. D. Frenkel, A. J. C. Ladd, *Phys. Rev. Lett.* **59**, 1169 (1987).
8. R. Hull, J. C. Bean, D. J. Werder, R. E. Leibenguth, *Appl. Phys. Lett.* **52**, 1605 (1988).
9. A. van Blaaderen, R. Ruel, P. Wiltzius, *Nature* **385**, 321 (1997).
10. The silica particles (Micromod, Sicastar, 1.5 μm) are suspended in an index-matching mixture of water and dimethyl sulfoxide at an initial volume fraction of 0.03%. We add a small amount of a fluorescein-NaOH mixture to the solvent, allowing us to image the particles with fluorescence under the confocal microscope; the particles appear as dark spheres in a light background.
11. We use standard photolithographic processes to prepare a template with a square array of 3000 by 3000 holes in a polymethyl methacrylate layer 500 nm thick over an area of about 5 mm by 5 mm.
12. For example, we estimate that increasing the film thickness from 20 μm to 30 μm produces a 0.4% decrease in the preferred lattice spacing.
13. D. B. Williams, C. B. Carter, *Transmission Electron Microscopy: A Textbook for Materials Science* (Plenum, New York, 1996).
14. D. Hull, D. J. Bacon, *Introduction to Dislocations* (Pergamon, New York, 1984).
15. S. Pronk, D. Frenkel, *J. Chem. Phys.* **110**, 4589 (1999).
16. F. C. Frank, J. H. van der Merwe, *Proc. R. Soc. London Ser. A* **198**, 216 (1949).
17. J. W. Matthews, A. E. Blakeslee, *J. Cryst. Growth* **27**, 118 (1974).
18. In accordance with the one-dimensional dislocation model, we assume that the $x$ and $y$ directions are uncoupled and study the accommodation of the misfit strain in one spatial direction. The elastic energy stored in a strained film of thickness $h$ is $U_{el} = \frac{1}{2}\varepsilon_{el}^2 Eh$ per unit area, where the elastic strain is $\varepsilon_{el} = \varepsilon_0 - \varepsilon$, and $\varepsilon$ is the strain relieved by the dislocations. The energy cost per unit area associated with the misfit dislocations is $U_l = (\Lambda^{-1})\{\mu b^2 \ln(R/r_c)/[4\pi(1-\nu)]\}$, where $b$ is the magnitude of the Burgers vector of the dislocations, and $r_c$ and $R$ are the core and outer radii of the dislocation strain field, respectively (*1*). Minimizing the total energy $U_{el} + U_l$ with respect to the number of dislocations per unit length $\Lambda^{-1}$, we find that, for film thicknesses greater than $h_c$, the equilibrium dislocation density is $\Lambda^{-1} = [\varepsilon_0/(b \cos\alpha)] - \{\mu \ln(R/r_c)/[4\pi(1-\nu)E \cos^2\alpha\, h]\}$. As the film thickness increases, the dislocation density approaches the limit $[\varepsilon_0/(b \cos\alpha)]$, where the entire misfit strain is accommodated by dislocations. The critical film thickness, where $\Lambda^{-1} = 0$, is $h_c = \mu b \ln(R/r_c)/[4\pi E\varepsilon_0(1-\nu)\cos\alpha]$; this yields a critical thickness $h_c = 22$ μm.
19. M. Jorand, F. Rothen, P. Pieranski, *J. Phys. (Paris)* **46**, 245 (1985).
20. We note that this value for the strain $\varepsilon$ is larger than that predicted for this 31-μm-thick film grown on a template where $\varepsilon_0 = 0.015$. However, the model prediction depends sensitively on the value of the misfit strain $\varepsilon_0$. For example, a 0.005 increase in the misfit strain can account for the discrepancy. Such an increase can result from the change in pressure head when the film thickness changes from 20 μm to 30 μm.
21. The elastic energy stored in the thin crystal layer below the dislocations is $U_{el} = \frac{1}{2}\varepsilon_0^2 Ez$ per area and decreases with decreasing distance, $z$, of the dislocations to the template. Hence, a single dislocation experiences the elastic force $F_{el} = \frac{1}{2}\Lambda E\varepsilon_0^2$.
22. J. W. Matthews, S. Mader, T. B. Light, *J. Appl. Phys.* **41**, 3800 (1970).
23. The forces acting on the screw dislocation are given by $F_{PK} = 2\mu(1+\nu)hb \cos\alpha\, \varepsilon_{el}/(1-\nu)$, $F_l = \mu b^2 \ln(R/r_c)/[4\pi(1-\nu)]$, and $F_d = (h/\sin\alpha)\gamma v$, where $\gamma = \eta b^2/4\pi r_c^2$, $v$ is the velocity of the screw dislocations, and $\eta$ is the solvent viscosity. As the dislocation expands, it accommodates an increasing portion of the misfit strain. The rate at which the strain is accommodated is $d\varepsilon/dt = \rho_{screw}\, b \cos\alpha\, v$, where $\rho_{screw}$ is the number of mobile screw dislocations per unit area of the film. From the force balance $F_{PK} = F_l + F_d$, we find that $\varepsilon(t) = \varepsilon_{inf}[1 - \exp(-t/\tau)]$, where the constant $\varepsilon_{inf} = \varepsilon_0 - \{b \ln(R/r_c)/[8\pi(1+\nu)h \cos\alpha]\}$ corresponds to the final misfit strain accommodated by the dislocation, and the time constant $\tau = (1-\nu)\gamma/(Eb^2 \cos^2\alpha \sin\alpha\, \rho_{screw})$. Because $\varepsilon$ is proportional to the dislocation length $L$, this equation predicts the time dependence of $L$. To calculate the elastic modulus from the measured time constant $\tau$, we determine the density of mobile screw dislocations by counting the number of dislocations that are expanding, multiplying by 2, and dividing by the area corresponding to the field of view. We obtain $\rho_{screw} = 3 \times 10^{-4}$ μm$^{-2}$. Taking $\eta = 3.0 \times 10^{-3}$ Pa·s (*24*), we obtain a value of 0.3 Pa for the elastic modulus.
24. Y. Higashigaki, D. H. Christensen, C. H. Wang, *J. Phys. Chem.* **85**, 2531 (1981).



25. We thank R. Christianson and D. Blair for their help with the image analysis, and E. Chen and Y. Lu for their help in manufacturing the templates. Supported by a Lynen Fellowship from the Alexander von Humboldt Foundation (P.S.), by NSF grant DMR-0243715, and by Harvard MRSEC grant DMR-0213805.


**Supporting Online Material**

www.sciencemag.org/cgi/content/full/305/5692/1944/DC1

Movie S1

30 June 2004; accepted 20 August 2004

# Ice Flow Direction Change in Interior West Antarctica

**Martin J. Siegert,[1]* Brian Welch,[2] David Morse,[3] Andreas Vieli,[1] Donald D. Blankenship,[3] Ian Joughin,[4] Edward C. King,[5] Gwendolyn J.-M. C. Leysinger Vieli,[1] Antony J. Payne,[1] Robert Jacobel[2]**

**Upstream of Byrd Station (West Antarctica), ice-penetrating radar data reveal a distinctive fold structure within the ice, in which isochronous layers are unusually deep. The fold has an axis more than 50 kilometers long, which is aligned up to 45° to the ice flow direction. Although explanations for the fold's formation under the present flow are problematic, it can be explained if flow was parallel to the fold axis ~1500 years ago. This flow change may be associated with ice stream alterations nearer the margin. If this is true, central West Antarctica may respond to future alterations more than previously thought.**

Ice-penetrating radar provides information on ice thickness, subglacial morphology, and internal layering, caused by electromagnetic-wave reflections from dielectric contrasts (such as high-acidity horizons formed from the aerosol product of volcanic events contained within ancient snow). Internal layers are believed to be isochronous, as